

Moiré Landau fans and magic zeros

Nisarga Paul,* Philip J.D. Crowley,* Trithep Devakul,* and Liang Fu
Department of Physics, Massachusetts Institute of Technology, Cambridge, MA, USA

We study the energy spectrum of moiré systems under a uniform magnetic field. The superlattice potential generally broadens Landau levels into Chern bands with finite bandwidth. However, we find that these Chern bands become flat at a discrete set of magnetic fields which we dub “magic zeros”. The flat band subspace is generally different from the Landau level subspace in the absence of the moiré superlattice. By developing a semiclassical quantization method and taking account of superlattice induced Bragg reflection, we prove that magic zeros arise from the simultaneous quantization of two distinct k -space orbits. For instance, we show the chiral model of TBG has flat bands at special fields for *any* twist angle in the n th Landau level for $|n| > 1$. The flat bands at magic zeros provide a new setting for exploring crystalline fractional quantum Hall physics.

The advent of moiré materials has opened a new regime for the study of Bloch electrons under a magnetic field [1–5]. Moiré materials feature a superlattice period that is much larger than the atomic spacing and can be comparable to the magnetic length at $B = 1\text{T}$ (26nm). Moreover, the superlattice potential that creates mini-bands is weak and slowly varying. As a result of both features, the interplay between Landau quantization and superlattice potential can give rise to a complex energy spectrum and novel quantum phenomena not found in ordinary solids [6–14].

In this work, we study the energy spectrum of two-dimensional moiré materials under a magnetic field B . Our work mainly focuses on the case of a superlattice potential not too strong relative to bandwidth such that the corresponding moiré bands can be treated by nearly free electron approximation. The energy spectrum as a function of magnetic field displays three distinct regimes. At very small magnetic fields, a set of Landau levels (LLs) arise from the standard semiclassical quantization [15] of cyclotron orbits that follow the constant energy contour of moiré bands. In the opposite limit of very large fields, a different set of LLs which come from “free” electrons without moiré effects are recovered. In the wide range of intermediate magnetic fields, the competition between magnetic breakdown and superlattice induced Bragg reflection at the mini Brillouin zone boundary leads to a new type of energy spectrum with remarkable universal features, which is the main finding of this work.

We develop a general method to calculate the Landau spectrum on the moiré superlattice. We show that at intermediate magnetic fields, the LLs of free electrons are generally broadened by Bragg scattering off the moiré superlattice, or in a complementary way, the LLs of Bloch electrons are broadened by magnetic breakdown near the mini Brillouin zone boundary. Remarkably, flat bands are found at a discrete set of magnetic fields, which we dub “magic zeros”. Plotted in the (B, μ) plane where μ is the chemical potential, each zero occurs at the intersection of two fictitious LL fans, corresponding to the simultaneous quantization of two distinct k -space orbits. The corresponding density of states divergence predicted by

our theory directly manifests as a peak in the compressibility $dn/d\mu$. Alternatively, LL widths can be measured directly by STM [12] and inferred from inter-LL optical transitions [16]. One application is chiral twisted bilayer graphene (TBG), which we find has magic zeros in LLs for $|n| > 1$ at *all* twist angles and not just the discrete set of magic angles [17].

Importantly, we show the existence of these flat bands is robust and not limited to the particular known case of Schrödinger or Dirac LLs perturbed by a weak potential $V_0 \ll \omega_c$ (with ω_c the cyclotron frequency) [18]. In contrast, our theory of magic zeros is non-perturbative in V_0/ω_c and applicable to generic energy dispersions. We show the flat band at a magic zero spans a Hilbert space that is generally distinct from the LL subspace of free electrons. The physics of flat bands at magic zeros contrasts and complements the broadening and Hofstadter-type splitting of LLs at generic B fields.

We consider a two-dimensional Bloch electron in a uniform magnetic field:

$$H = H_0(\mathbf{p} - e\mathbf{A}) + V(\mathbf{r}) \quad (1)$$

where $H_0(\mathbf{p})$ denotes the energy dispersion in the absence of moiré superlattice and \mathbf{A} is the vector potential.

$$V(\mathbf{r}) = \sum_{\mathbf{q}} V(\mathbf{q}) e^{i\mathbf{q}\cdot\mathbf{r}} + c.c. \quad (2)$$

denotes a periodic moiré potential ($\hbar = 1$). As the superlattice potential in moiré materials is slowly varying, $V(\mathbf{r})$ is well approximated as a sum of a few lowest leading harmonics.

Depending on the form of H_0 and V , H describes a wide variety of moiré materials. In the case of semiconductor transition metal dichalcogenide (TMD) heterostructures such as WSe_2/WS_2 , $H_0(\mathbf{p}) = p^2/2m$ where m is the effective mass near the band edge of TMD monolayer, and the triangular symmetric potential $V(\mathbf{r})$ is composed of three Fourier components of equal magnitude at wavevectors related by symmetry [19]. In the case of graphene on a one-dimensional patterned dielectric superlattice, $H_0(\mathbf{p}) = v\mathbf{p} \cdot \boldsymbol{\sigma}$ is the Dirac Hamiltonian of graphene, and $V(\mathbf{r}) = V_0 \cos(qx)$ involves a single

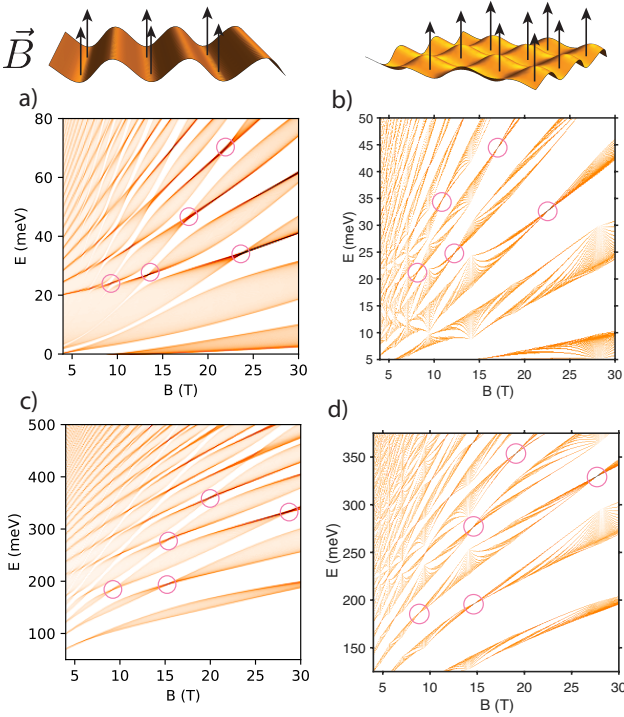


FIG. 1. DOS in a periodic potential and magnetic field for Schrödinger (a,c) and Dirac (b,d) electrons. A few prominent “magic zeros” are circled, robust features where the bandwidth vanishes. (a,b) Exact diagonalization for a 1D periodic potential. (c,d) Perturbative results for a 2D six-fold symmetric potential. Parameters: (a) $V_0 = 15$ meV, $m^* = 0.2m_e$, (b) $V_0 = 70$ meV, $v = 10^6$ m/s, (c) $V_0 = 4$ meV, $m^* = 0.2m_e$, (d) $V_0 = 25$ meV, $v = 10^6$ m/s. Period $a = 13$ nm.

wavevector only [6]. In both cases, the periodic potential $V(\mathbf{r})$ results in mini-bands, as manifested in resistive peaks at commensurate densities. Under a magnetic field, transport measurements observed complex patterns in the LL spectra.

The first indication of magic zeros can be found in the regime where the superlattice potential strength is smaller than the cyclotron energy ω_c of free electrons [18]. In this perturbative regime, $V(\mathbf{r})$ lifts the infinite degeneracy within a LL. The projection of periodic potential into the n th LL of Schrödinger electrons can then be written [18, 20] (choosing symmetric gauge $\mathbf{A} = \frac{1}{2}\mathbf{B} \times \mathbf{r}$)

$$V_n^{\text{eff}} = \sum_{\mathbf{q}} V(\mathbf{q}) e^{-q^2 l_B^2/4} L_n(q^2 l_B^2/2) e^{i\mathbf{q} \cdot (-\tilde{\pi}_y, \tilde{\pi}_x) l_B^2} \quad (3)$$

where $l_B = 1/\sqrt{eB}$ is the magnetic length, $\tilde{\pi} = \mathbf{p} + e\mathbf{A}$, and L_n is the n th Laguerre polynomial. Note $[\tilde{\pi}_x, \tilde{\pi}_y] = -ieB$. Notably, when all wavevectors are of equal magnitude q , the LL projected potential in Eq. (3) vanishes at n values of ql_B due to the Laguerre polynomial zeros, leading to a flat Chern band despite the presence of periodic potential. In the case of Dirac electrons, the n th LL wavefunction is a two-component spinor and the pro-

$ n $	ql_B (Schrödinger case)	ql_B (Dirac case)
1	$\sqrt{2}$	2
2	1.08, 2.61	1.24, 3.24
3	0.91, 2.14, 3.55	0.99, 2.36, 4.18
4	0.80, 1.87, 3.01, 4.34	0.86, 2, 3.26, 4.96
5	0.73, 1.68, 2.68, 3.77, 5.03	0.76, 1.77, 2.84, 4.03, 5.65

TABLE I. Values of ql_B for which the n th LL has zero bandwidth for weak potential, where q is the potential wavevector and l_B the magnetic length, for Schrödinger and Dirac electrons. The n th level exhibits $|n|$ magic zeros.

jected potential is given by [21]: $\tilde{V}_n^{\text{eff}} = (V_{|n|}^{\text{eff}} + V_{|n|-1}^{\text{eff}})/2$ for $n \neq 0$. Zeros occur in this case as well. Magic zeros for the first few LLs are listed in Table I, and the perturbative spectrum for a six-fold symmetric potential is shown in Fig. 1c-d.

Remarkably, we find that the magic zeros persist beyond the perturbative regime, as indicated by the exact diagonalization (ED) of the energy spectrum of Eq. (1) in Fig. 1a-b for the case of a potential $V_0 \cos(qx)$. At the density of states (DOS) peaks shown, the bandwidth is zero within numerical accuracy, even in the regime $V_0/\omega_c \sim 3$. This result is truly all-orders in V_0/ω_c , as indicated by the following: (i) magic zeros deviate from the Laguerre polynomial zeros and (ii) the wavefunction at the zeros differs from the LL wavefunction at $V(\mathbf{r}) = 0$ (see SM).

In order to uncover the origin of these zeros, we develop a semiclassical approach which places no restrictions on V_0/ω_c . Moreover, this approach does not rely on a specific form of energy dispersion $H_0(\mathbf{p})$, and thus is applicable to a wider range of systems, such as bilayer graphene with trigonal warping. The starting point for the semiclassics is to consider a Bloch wavepacket whose position and momentum are governed by the equations

$$\dot{\mathbf{p}} = -e\dot{\mathbf{r}} \times \mathbf{B}, \quad \dot{\mathbf{r}} = \nabla E(\mathbf{p}), \quad (4)$$

where $E(\mathbf{p})$ is the energy dispersion *including* the effect of the periodic potential.

When the potential $V(\mathbf{r})$ is absent, electrons at an energy ε follow the original Fermi surface $H_0(\mathbf{p}) = \varepsilon$. When the potential is strong, electrons follow the reconstructed Fermi surface $E(\mathbf{p}) = \varepsilon$ where \mathbf{p} lies in the mini Brillouin zone. In both cases, semiclassical quantization predicts infinitely degenerate LLs whenever the real-space orbits, which are simply \mathbf{p} -space orbits rotated by $\pi/2$ and scaled by $1/B$, enclose integer flux [15].

In between these two limits, magnetic breakdown [22–24] broadens the LLs. Let us consider an intersection of two original Fermi surfaces at the first Bragg plane in the repeated-zone scheme. In a magnetic field, there are two incoming and two outgoing electron wavepackets. Thus we may treat the intersection as a two-level Landau-

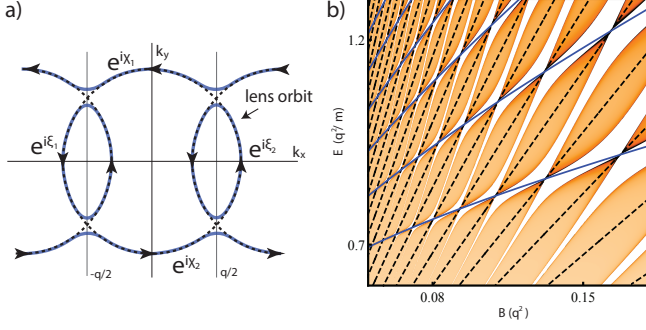


FIG. 2. (a) Fermi surface in the repeated zone scheme in the presence of a 1D potential $V_0 \cos(qx)$. The network model (dashed lines) involves scattering at intersections and phases picked up on links. (b) Intersecting Landau fans due to the original orbit (dashed lines) and lens orbit (blue), and semi-classical DOS (density plot) with $V_0 = 0.4$, $q = 2$, $m = 1$.

Zener system with a scattering matrix U . When B is sufficiently small, electrons follow on the reconstructed Fermi surface and occasionally break through, and U is mainly diagonal. When B is large, electrons follow the original Fermi surface and occasionally Bragg scatter, so U is mainly off-diagonal.

In general, the scattering matrix takes the form

$$U = \begin{pmatrix} \sqrt{1-P}e^{-i\tilde{\varphi}_S} & -\sqrt{P} \\ \sqrt{P} & \sqrt{1-P}e^{i\tilde{\varphi}_S} \end{pmatrix} \quad (5)$$

where the magnetic breakdown probability is

$$P = e^{-2\pi/\delta}, \quad \delta = 16eBv_1v_2 \sin \alpha / E_{\text{gap}}^2, \quad (6)$$

v_1 and v_2 are incoming electron velocities which differ by an angle α , $E_{\text{gap}} = 2V_0$ is the band gap at the Bragg plane, and $\tilde{\varphi}_S = \varphi_S - \pi/2$ with $\varphi_S = \pi/4 - (\ln \delta + 1)/\delta + \arg \Gamma(1 - i/\delta)$, the so-called Stokes phase [22, 25] (see SM). We note $e^{-i\tilde{\varphi}_S}$ only depends weakly on δ , interpolating between i and $i^{1/2}$. Eqs. (5) and (6) are derived using the nearly free electron approximation assuming that the effect of the potential on the band structure is only significant near Brillouin zone boundary. Note that P goes to zero quickly at low fields and approaches 1 at high fields.

In the case of parabolic bands, δ reduces to $8\varepsilon\omega_c \sin \alpha / V_0^2$. For bilayer TMDs with $\varepsilon \sim 20$ to 40 meV, $q \sim k_F$ (k_F is the Fermi wavevector), and $\omega_c \sim 2$ meV at 10 T, $P \sim 0.1$ to 0.3. For graphene in a 1D potential [6], taking $V_0 a / v_F \sim 1$ to 10, $a \sim 50$ nm, $q \sim k_F$, and $B \sim 10$ T gives $P \sim 0.01$ to 0.95. Evidently, realistic values of P in moiré materials require that the effects of magnetic breakdown are properly taken into account.

To properly account for magnetic breakdown, we consider a network model comprised of the original Fermi surfaces in the repeated zone scheme where wavepacket motion away from the intersections is free electron-like

while scattering at the intersections is given by the Landau-Zener unitary U . Let us first consider networks in which neighboring Fermi surface intersect at two points as in Fig. 2a. This is similar in spirit to models considered by Pippard [26, 27]; we refer to [28–30] for other examples of network model constructions. We refer to the original Fermi surfaces defined by $H_0(\mathbf{p}) = \varepsilon$ as the “original orbit” and their intersection as the “lens orbit”.

To understand the magic zero condition in the semiclassical approach, it is instructive to consider the scattering matrix across a lens orbit, which is given by

$$W = \frac{1}{(1-P)e^{i(\xi_1+\xi_2+2\tilde{\varphi}_S)} - 1} \begin{pmatrix} Pe^{i\xi_1} & \kappa \\ \kappa & Pe^{i\xi_2} \end{pmatrix} \quad (7a)$$

$$\kappa = e^{-i\tilde{\varphi}_S} \sqrt{1-P} (e^{i(\xi_1+\xi_2+2\tilde{\varphi}_S)} - 1), \quad (7b)$$

where ξ_1, ξ_2 are the phases acquired along the links of the lens orbit. W describes scattering between incoming and outgoing states across the lens orbit. When W is diagonal, incoming states scatter into outgoing states in the same zone.

We note that when $\xi_1 + \xi_2 + 2\tilde{\varphi}_S$ is an integer multiple of 2π , W is diagonal, indicating the decoupling of neighboring orbits in the network. This is reminiscent of constructive interference in a Fabry-Pérot optical cavity [8, 31], where the lens orbit plays the role of the cavity. The decoupled orbits are valid eigenstates when the phase around the original orbit is an integer multiple of 2π . Under these conditions, the network model supports an extensive set of states which are localized and dispersionless, i.e. a flat band.

In brief, the flat band conditions, in terms of the phases shown in Fig. 2a, are $\sum \xi_i + 2\tilde{\varphi}_S \in 2\pi\mathbb{Z}$ and $\sum(\xi_i + \chi_i) \in 2\pi\mathbb{Z}$. The phases satisfy:

$$\sum_{\text{orig}} \xi_i + \chi_i = l_B^2 S_0 + 2\pi\gamma, \quad \sum_{\text{lens}} \xi_i = l_B^2 S_1 + 2\pi\gamma \quad (8)$$

where S_0, S_1 are the \mathbf{p} -space areas of the original and lens orbits, respectively. We have added the topological Maslov contribution $\gamma = 1/2 - \varphi_{\text{Berry}}/2\pi$ which is customary in semiclassical treatments for closed orbits deformable to a circle [32–35], with Schrödinger and Dirac electrons having $\gamma = 1/2$ and 0 respectively. φ_{Berry} is the Berry phase along the orbit.

Combining the above conditions, we find that band-width zeros occur at the intersection of the two Landau fans given by

$$l_B^2 S_0 = 2\pi(n + \gamma) \quad (9a)$$

$$l_B^2 S_1 = 2\pi(m + \gamma - \tilde{\varphi}_S/\pi) \quad (9b)$$

for suitable integers m, n . These equations stipulate that both the original and lens orbits enclose integer flux, up to the Stokes phase and Maslov correction. The magic

zero conditions, i.e. Eq. (9), can be roughly thought of as Bohr-Sommerfeld quantization conditions for both the original and lens orbits. In general, a sufficient condition for magic zeros is a Fermi contour with only *two* relevant independent semiclassical electron orbits (with other orbit areas integer linear combinations of these). For circular Fermi surfaces, these two areas are

$$S_0 = \pi k_F^2, \quad S_1 = 2k_F^2(\cos^{-1} x - x\sqrt{1-x^2}), \quad (10)$$

where $x = q/2k_F$. For this case the intersecting Landau fans are shown in Fig. 2b.

In the large n and weak potential limit, the semiclassical and perturbative approaches are expected to agree. Eq. (10) and Eq. (9a) give $k_F^2 = 2(n + \gamma)/l_B^2$. Applying this to Eqs. (9b) and (10) and noting $\tilde{\varphi}_S/\pi \rightarrow -1/4$ at weak potential, the values of ql_B at which the n th LL has a magic zero are given by

$$ql_B = \frac{\pi(n - m - 1/4)}{\sqrt{2n}} + O(n^{-1}) \quad (11)$$

for integers m, n . In the perturbative regime, Eq. (3) implies that these are the zeros of $L_n(q^2 l_B^2/2)$. Indeed, by applying the large n formula [36]

$$e^{-\frac{q^2 l_B^2}{4}} L_n(q^2 l_B^2/2) = \frac{\cos(\sqrt{2n}ql_B - \frac{\pi}{4})}{\sqrt{\pi ql_B \sqrt{n/2}}} + O(n^{-\frac{3}{4}}), \quad (12)$$

we see that these magic zero conditions derived independently are identical. We remark that the phenomenon of Weiss oscillations [8, 18, 37–40]—superlattice induced magnetoresistance oscillations—is naturally captured by the semiclassical approach in this regime (see SM).

So far we have only discussed magic zeros, but the network model also allows us to calculate the band dispersion at generic fields using a transfer matrix approach. For the network in Fig. 2 due to a 1D potential (we defer discussion of the 2D case), the transfer matrix eigenvalues $e^{\pm i\theta}$ satisfy the relation

$$\cos \theta = \frac{\sin(\xi + \chi) + (1 - P) \sin(\xi - \chi + 2\tilde{\varphi}_S)}{2\sqrt{1 - P} \sin(\xi + \tilde{\varphi}_S)} \quad (13)$$

where a gauge choice such that $\xi_1 = \xi_2 = \xi$ and $\chi_1 = \chi_2 = \chi$ has been made. The resulting semiclassical spectrum is shown in Fig. 2b. We show the quantitative agreement with ED in the SM. The LLs alternately broaden and pinch off at magic zeros, and the corresponding DOS divergences directly manifest as peaks in compressibility $dn/d\mu$ (see e.g. Fig. 3b and the SM). Importantly, we have placed no restrictions on V_0/ω_c , so our results are all-orders in conventional perturbation theory. Moreover, our treatment did not depend on the precise energy dispersion, and a different dispersion would only alter geometric details such as Fermi surface areas and link phases. The existence of magic zeros, which is our main focus, is robust to all these details.

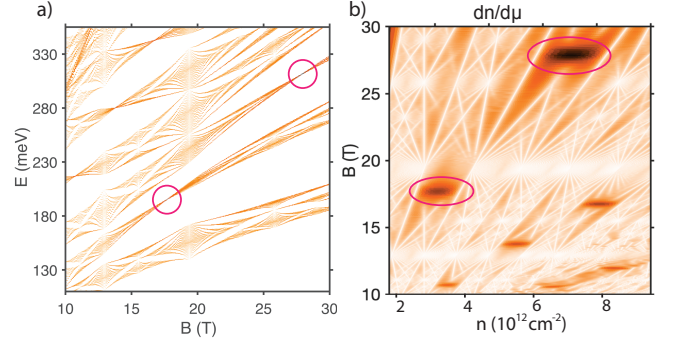


FIG. 3. (a) DOS for chiral limit TBG with $V_0 = 30$ meV, $v = 10^6$ m/s at $\theta = 1.1^\circ$. Zeros exist at any twist angle. (b) Noninteracting compressibility as a function of density and B at $T = 0.2$ meV. Magic zeros are dark features of high compressibility occurring over a finite range of n .

So far we have assumed the Fermi surface intersects only a single pair of Bragg planes at $\pm q\hat{x}/2$. In moiré materials made of highly doped semiconductors or metals, however, $V(\mathbf{r})$ may have a small wavevector compared to the size of the Fermi surface, resulting in a network many overlaps. An important simplification is that the gaps at the intersections form a distinct hierarchy with $E_{\text{gap}}^{\text{th}} \sim V_0^n/(v_F k_F)^{n-1}$ at an n th order Bragg plane. Therefore P has a double-exponential dependence on n and only a few crossings are active, with the rest completely avoided ($P = 0$) or trivial ($P = 1$). The simplest scenario is when only the intersections at the first-order Bragg plane are active. From Eq. (6), for the parabolic case this requires $V_0^4/(v_F k_F)^3 \ll \omega_c \sin \alpha_2, V_0^2/v_F k_F \ll \omega_c \sin \alpha_1$ where α_j is the intersection angle at the j th Bragg plane (and $\alpha_1 \approx \alpha_2$ when intersections are close together). In this “first-order regime” [41], the network model maps exactly back onto the simplest case of a single intersection, Fig. 2a. Therefore the DOS plot is the same as before, albeit with a slightly restricted regime of validity.

Let us discuss the extension to 2D potentials, such as a triangular lattice potential. Strictly speaking, the network model approach is only valid when φ , the number of flux quanta per real-space unit cell, is a rational number p/q ; then the network unit cell is enlarged by a factor of p and each LL contains p subbands (for coprime p, q) [27]. However, if the enlarged unit cell consists of only original and lens orbits, they decouple when W becomes diagonal, and the flux at a magic zero can be approximated arbitrarily well by a rational φ . Thus magic zeros arise in this case with identical conditions. When the network topology has overlapping lens orbits, we conjecture that magic zeros still arise (see SM). For magic zeros to arise, the lens orbits of the network model must have equal areas, which requires wavevectors of equal magnitude. This is consistent with the perturbative result of Eq. (3).

We underscore a few necessary conditions for magic zeros which are frequently satisfied in moiré materials: (1) a superlattice potential consisting of equal-magnitude wavevectors must be present, (2) the Fermi surface must be invariant under the rotational symmetry of the potential, and (3) the potential is not so strong as to significantly restructure the bandstructure. Perturbations which would broaden magic zeros include higher order harmonics, strain, or anisotropic dispersions.

A natural question is whether TBG [42, 43] exhibits magic zeros. While our theory based on a scalar moiré potential does not apply directly, we find magic zeros exist in the chiral limit [17] at *any* twist angle; we plot the noninteracting perturbative DOS and compressibility in Fig. 3 and include details in the SM.

The flat Chern band at magic zeros provides an ideal setting for realizing fractional quantum Hall (FQH) states and other novel states at fractional fillings. For instance, the increased bandwidth away from magic zeros weakens the Laughlin state and may induce a transition into metallic states or electron crystals. We leave these directions to future work.

Acknowledgments— We thank Ray Ashoori and Long Ju for helpful discussions. This work is supported by a Simons Investigator Award from the Simons Foundation and the STC Center for Integrated Quantum Materials (CIQM) under NSF award no. ECCS-2025158. LF is partly supported by the David and Lucile Packard Foundation.

* These authors contributed equally

- [1] D. J. Thouless, M. Kohmoto, M. P. Nightingale, and M. Den Nijs, *Phys. Rev. Lett.* **49**, 405 (1982).
- [2] P. G. Harper, *Proc. Phys. Soc. A* **68**, 874 (1955).
- [3] D. R. Hofstadter, *Phys. Rev. B* **14**, 2239 (1976).
- [4] M. Wilkinson, *Proceedings of the Royal Society of London. A. Mathematical and Physical Sciences* **391**, 305 (1984).
- [5] R. Bistritzer and A. H. MacDonald, *Phys. Rev. B* **84**, 035440 (2011).
- [6] Y. Li, S. Dietrich, C. Forsythe, T. Taniguchi, K. Watanabe, P. Moon, and C. R. Dean, *Nat. Nanotechnol.* **16**, 525 (2021).
- [7] C. Forsythe, X. Zhou, K. Watanabe, T. Taniguchi, A. Pasupathy, P. Moon, M. Koshino, P. Kim, and C. R. Dean, *Nat. Nanotechnol.* **13**, 566 (2018).
- [8] M. Drienovsky, J. Joachimsmeier, A. Sandner, M.-H. Liu, T. Taniguchi, K. Watanabe, K. Richter, D. Weiss, and J. Eroms, *Phys. Rev. Lett.* **121**, 026806 (2018).
- [9] R. Huber, M.-H. Liu, S.-C. Chen, M. Drienovsky, A. Sandner, K. Watanabe, T. Taniguchi, K. Richter, D. Weiss, and J. Eroms, *Nano Lett.* **20**, 8046 (2020).
- [10] B. Hunt, J. D. Sanchez-Yamagishi, A. F. Young, M. Yankowitz, B. J. LeRoy, K. Watanabe, T. Taniguchi, P. Moon, M. Koshino, P. Jarillo-Herrero, and R. C. Ashoori, *Science* (2013).
- [11] C. R. Dean, L. Wang, P. Maher, C. Forsythe, F. Ghahari, Y. Gao, J. Katoch, M. Ishigami, P. Moon, M. Koshino, T. Taniguchi, K. Watanabe, K. L. Shepard, J. Hone, and P. Kim, *Nature* **497**, 598 (2013).
- [12] Y. Okada, W. Zhou, C. Dhital, D. Walkup, Y. Ran, Z. Wang, S. D. Wilson, and V. Madhavan, *Phys. Rev. Lett.* **109**, 166407 (2012).
- [13] E. M. Spanton, A. A. Zibrov, H. Zhou, T. Taniguchi, K. Watanabe, M. P. Zaletel, and A. F. Young, *Science* (2018).
- [14] B. Andrews and A. Soluyanov, *Phys. Rev. B* **101**, 235312 (2020).
- [15] L. Onsager, *London, Edinburgh, and Dublin Philosophical Magazine and Journal of Science* **43**, 1006 (1952).
- [16] L. Ju, L. Wang, T. Cao, T. Taniguchi, K. Watanabe, S. G. Louie, F. Rana, J. Park, J. Hone, F. Wang, and P. L. McEuen, *Science* (2017).
- [17] G. Tarnopolsky, A. J. Kruchkov, and A. Vishwanath, *Phys. Rev. Lett.* **122**, 106405 (2019).
- [18] D. Pfannkuche and R. R. Gerhardt, *Phys. Rev. B* **46**, 12606 (1992).
- [19] C. Jin, E. C. Regan, A. Yan, M. Iqbal Bakti Utama, D. Wang, S. Zhao, Y. Qin, S. Yang, Z. Zheng, S. Shi, K. Watanabe, T. Taniguchi, S. Tongay, A. Zettl, and F. Wang, *Nature* **567**, 76 (2019).
- [20] M. Wilkinson, *Journal of Physics A: Mathematical and General* **20**, 1761 (1987).
- [21] R. Huber, M.-N. Steffen, M. Drienovsky, A. Sandner, K. Watanabe, T. Taniguchi, D. Pfannkuche, D. Weiss, and J. Eroms, *arXiv* (2021), 2106.11328.
- [22] E. I. Blount, *Phys. Rev.* **126**, 1636 (1962).
- [23] M. H. Cohen and L. M. Falicov, *Phys. Rev. Lett.* **7**, 231 (1961).
- [24] J. R. Reitz, *J. Phys. Chem. Solids* **25**, 53 (1964).
- [25] S. N. Shevchenko, S. Ashhab, and F. Nori, *Phys. Rep.* **492**, 1 (2010).
- [26] A. B. Pippard, *Proc. R. Soc. London A - Math. Phys. Sci.* **270**, 1 (1962).
- [27] A. B. Pippard, *Philosophical Transactions of the Royal Society of London. Series A, Mathematical and Physical Sciences* **256**, 317 (1964).
- [28] Y.-Z. Chou, F. Wu, and S. Das Sarma, *Phys. Rev. Research* **2**, 033271 (2020).
- [29] W. G. Chambers, *Phys. Rev.* **140**, A135 (1965).
- [30] R. G. Chambers, *Proc. Phys. Soc.* **88**, 701 (1966).
- [31] M. Drienovsky, F.-X. Schrettenbrunner, A. Sandner, D. Weiss, J. Eroms, M.-H. Liu, F. Tkatschenko, and K. Richter, *Phys. Rev. B* **89**, 115421 (2014).
- [32] D. Xiao, M.-C. Chang, and Q. Niu, *Rev. Mod. Phys.* **82**, 1959 (2010).
- [33] J. B. Keller, *Ann. Phys.* **4**, 180 (1958).
- [34] G. P. Mikitik and Yu. V. Sharlai, *Phys. Rev. Lett.* **82**, 2147 (1999).
- [35] J. N. Fuchs, F. Piéchon, M. O. Goerbig, and G. Montambaux, *Eur. Phys. J. B* **77**, 351 (2010).
- [36] G. Szego, *Orthogonal polynomials*, 4th ed., Amer. Math. Soc. Colloq. Publ., Vol. 23 (American Mathematical Society, 1975).
- [37] R. R. Gerhardt, D. Weiss, and K. v. Klitzing, *Phys. Rev. Lett.* **62**, 1173 (1989).
- [38] C. Zhang and R. R. Gerhardt, *Phys. Rev. B* **41**, 12850 (1990).
- [39] P. Steda and A. H. MacDonald, *Phys. Rev. B* **41**, 11892 (1990).

- [40] C. W. J. Beenakker, Phys. Rev. Lett. **62**, 2020 (1989).
- [41] S. Spurrier and N. R. Cooper, Phys. Rev. B **100**, 081405 (2019).
- [42] R. Bistritzer and A. H. MacDonald, Proc. Natl. Acad. Sci. U.S.A. **108**, 12233 (2011).
- [43] Y. Cao, V. Fatemi, S. Fang, K. Watanabe, T. Taniguchi, E. Kaxiras, and P. Jarillo-Herrero, Nature **556**, 43 (2018).

Supplemental Material

Nisarga Paul,* Philip J.D. Crowley,* Trithep Devakul,* and Liang Fu
Department of Physics, Massachusetts Institute of Technology, Cambridge, MA, USA

WAVEFUNCTIONS AT MAGIC ZEROS

For a dispersion $p^2/2m$ with Landau gauge $\mathbf{A} = Bxy$, Landau level wavefunctions take the form

$$\psi_{n,p_y}(x, y) \sim e^{ip_y y} H_n(x - p_y l_B^2) e^{-(x - p_y l_B^2)^2/2l_B^2} \quad (1)$$

and have a mean position $\langle x \rangle = p_y l_B^2$. In Fig. 1, we plot the wavefunctions after including a periodic potential $V_0 \cos qx$. At generic fields, $\langle x \rangle$ has a nonlinear dependence on p_y while at magic zeros, a linear dependence $\langle x \rangle \sim p_y$ is recovered. However, the wavefunctions at a magic zero span a subspace distinct from the Landau level subspace spanned by free electron wavefunctions, which is clear because Fig. 1b corresponds to a functional form distinct from Eq. (1).

DETAILS OF THE SEMICLASSICAL MODEL

Scattering between bands as a Landau-Zener effect. In this section we present the mapping of a wavepacket scattering between two bands at an avoided crossing to a Landau-Zener problem, rectifying the original derivation in Ref. [?]. Consider a wavepacket in \mathbf{k} -space prepared initially in a single band with dispersion $E(\mathbf{k})$. In the presence of a magnetic field this wavepacket moves along the equipotentials of the dispersion. Consider introducing a periodic modulation in the extended zone scheme so

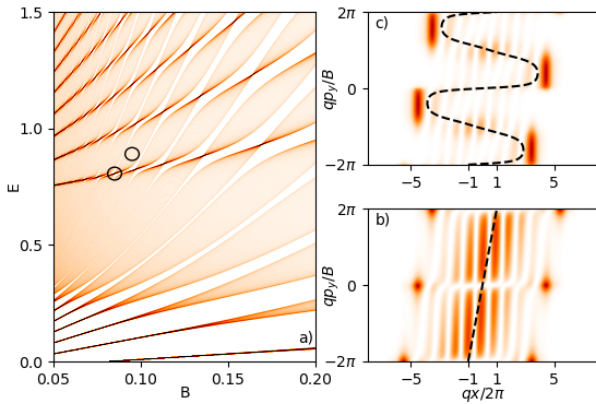


FIG. 1. (a) Density of states from exact diagonalization for parabolic dispersion $p^2/2m$ and periodic potential $V_0 \cos(qx)$ with $V_0 = 0.4, q = 2$ and $m = 1$. (b) Each horizontal line cut shows the Landau gauge wavefunction profile at a given momentum p_y away from a magic zero and (c) at a magic zero. The dashed line shows $\langle x \rangle$.

we have states at all momenta $E(\mathbf{k} + \mathbf{g})$ where \mathbf{g} is any reciprocal lattice vector. Consider two bands $E_1(\mathbf{k}) = E(\mathbf{k} + \mathbf{g}_1)$, $E_2(\mathbf{k}) = E(\mathbf{k} + \mathbf{g}_2)$, which are (naïvely) degenerate at the point \mathbf{k}^* , so that $E^* = E_1(\mathbf{k}^*) = E_2(\mathbf{k}^*)$. This degeneracy is ultimately split by a matrix element V , so that in the vicinity of \mathbf{k}^* we have the Hamiltonian

$$H = \begin{pmatrix} E_1(\mathbf{k}) & V \\ V & E_2(\mathbf{k}) \end{pmatrix} \quad (2)$$

As the wave-packet passes through \mathbf{k}^* it has some amplitude for scattering from one band to the other, an effect captured by the a 2×2 scattering matrix U . First we include minimal coupling $\mathbf{k} \rightarrow \mathbf{p} = \mathbf{k} - e\mathbf{A}$, and linearise the Hamiltonian about \mathbf{k}^*

$$H = \begin{pmatrix} E^* + \mathbf{v}_1 \cdot \mathbf{p} & V \\ V & E^* + \mathbf{v}_2 \cdot \mathbf{p} \end{pmatrix} \quad (3)$$

where $\mathbf{v}_n = \nabla_{\mathbf{k}} E_n(\mathbf{k})|_{\mathbf{k}=\mathbf{k}^*}$. This may be written in terms of Pauli as matrices as

$$H = E^* + (\mathbf{v}_+ \cdot \mathbf{p}) + V\sigma_x + (\mathbf{v}_- \cdot \mathbf{p})\sigma_z \quad (4)$$

where $\mathbf{v}_{\pm} = \frac{1}{2}(\mathbf{v}_1 \pm \mathbf{v}_2)$. We transform to the rotating frame $|\psi'\rangle = e^{iXt}|\psi\rangle$ with $X = E^* + \mathbf{v}_+ \cdot \mathbf{p}$ yielding the effective Hamiltonian

$$H' = V\sigma_x + (\mathbf{v}_- \cdot \mathbf{p} + ut)\sigma_z \quad (5)$$

where we have defined the constant u via the relation

$$u = i[\mathbf{v}_- \cdot \mathbf{p}, \mathbf{v}_+ \cdot \mathbf{p}] = e\mathbf{B} \cdot (\mathbf{v}_- \times \mathbf{v}_+). \quad (6)$$

We are now at liberty to work in the diagonal basis of $\mathbf{v}_- \cdot \mathbf{p}$, so that $\mathbf{v}_- \cdot \mathbf{p}$ is replaced with its eigenvalue, which may be absorbed by a redefinition of the origin of time to yield

$$H' = V\sigma_x + ut\sigma_z, \quad (7)$$

the textbook Landau-Zener Hamiltonian [? ?]. The Landau-Zener problem is characterised entirely by the dimensionless velocity

$$\left| \frac{u}{V^2} \right| = \frac{2eBv_1v_2 \sin \alpha}{V^2} \quad (8)$$

where α is the angle between \mathbf{v}_1 and \mathbf{v}_2 . We note the recovery of the expected ratio for parabolic bands

$$\left| \frac{u}{V^2} \right| = \frac{4E_F\omega_c \sin \alpha}{V^2} \quad (9)$$

where $E_F = mv_F^2/2$ is the Fermi energy and $\omega_c = eB/m$ is the cyclotron frequency.

Unitary scattering matrix U . The instantaneous eigenvalues of Eq. (7) are $E_{\pm} = \pm\sqrt{\Delta^2 + u^2 t^2}$. The corresponding instantaneous eigenvectors ϕ_{\pm} are only defined up to a (possibly time-dependent) phase. We choose a reasonable convention in which $\lim_{t \rightarrow -\infty} \phi_- = \lim_{t \rightarrow \infty} \phi_+$ and $\lim_{t \rightarrow -\infty} \phi_+ = \lim_{t \rightarrow \infty} \phi_-$. Then the appropriate unitary describing the Landau-Zener transition in this basis is [?]]

$$U = \begin{pmatrix} \sqrt{1-P}e^{-i\tilde{\varphi}_S} & -\sqrt{P} \\ \sqrt{P} & \sqrt{1-P}e^{i\tilde{\varphi}_S} \end{pmatrix} \quad (10)$$

where the magnetic breakdown probability is

$$P = e^{-2\pi/\delta}, \quad \delta = 4eBv_1v_2 \sin \alpha / V^2, \quad (11)$$

and $\tilde{\varphi}_S = \varphi_S - \pi/2$ with $\varphi_S = \pi/4 - (\ln \delta + 1)/\delta + \arg \Gamma(1 - i/\delta)$, the so-called Stokes phase. The Stokes phase is essential in recovering zeros in the perturbative limit and was missed by other semiclassical treatments as far as we know.

Unitary across a lens orbit W . Let us derive the unitary matrix W describing scattering across a lens orbit. We define various amplitudes in Fig. 2a. We seek the matrix satisfying

$$W \begin{pmatrix} \alpha_{\text{in}} \\ \beta_{\text{in}} \end{pmatrix} = \begin{pmatrix} \alpha_{\text{out}} \\ \beta_{\text{out}} \end{pmatrix} \quad (12)$$

where the intersections impose the relations

$$U \begin{pmatrix} \alpha_{\text{in}} \\ \phi_2 \end{pmatrix} = \begin{pmatrix} \beta_{\text{out}} \\ \phi_1 e^{-i\xi_1} \end{pmatrix} \quad \text{and} \quad U \begin{pmatrix} \beta_{\text{in}} \\ \phi_1 \end{pmatrix} = \begin{pmatrix} \alpha_{\text{out}} \\ \phi_2 e^{-i\xi_2} \end{pmatrix}. \quad (13)$$

After explicit calculation we arrive at

$$W = \frac{1}{(1-P)e^{i(\xi_1+\xi_2+2\tilde{\varphi}_S)} - 1} \begin{pmatrix} Pe^{i\xi_1} & \kappa \\ \kappa & Pe^{i\xi_2} \end{pmatrix} \quad (14a)$$

$$\kappa = e^{-i\tilde{\varphi}_S} \sqrt{1-P} (e^{i(\xi_1+\xi_2+2\tilde{\varphi}_S)} - 1), \quad (14b)$$

Note that the basis we have chosen implies that when W is diagonal, the amplitudes in different unit cells are decoupled. This occurs when $P = 1$ (total magnetic breakdown) or when $\xi_1 + \xi_2 + 2\tilde{\varphi}_S \in 2\pi\mathbb{Z}$. The latter condition, combined with the quantization condition $\xi_1 + \xi_2 + \chi_1 + \chi_2 \in 2\pi\mathbb{Z}$ for the full phase winding around the Fermi surface, implies a perfectly flat Chern band in the semiclassical model.

The flat band wavefunctions, however, are generally not homogeneous along the orbit as would be the case for bona fide Landau levels. Rather, the density accumulates along the lens orbit due to the constructive interference of multiple reflections, suggesting a quantum analog of a Fabry-Pérot optical cavity bound state. This is another way of seeing that the Hilbert space spanned

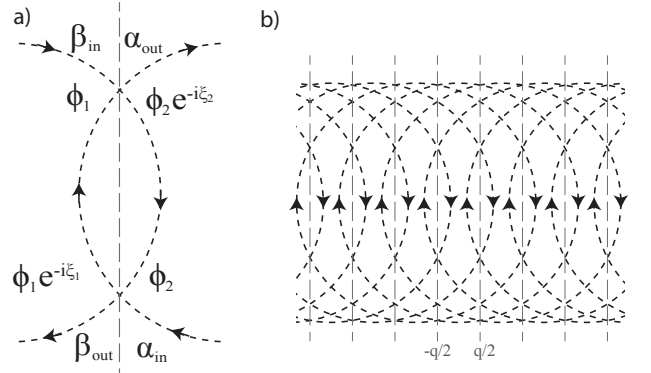


FIG. 2. (a) Defining the amplitudes in the lens orbit, relevant for the derivation of the unitary W . (b) Network model when many Fermi surfaces overlap.

by a magic zero is distinct from the free electron Landau level subspace.

In the limit $P \rightarrow 0$, W is entirely off-diagonal with phase i , which is just the expected Maslov correction for turning points [? ? ? ?]. In this limit the network decouples into open orbits along the top and bottom and closed lens orbits.

Density of states, 1D network. There is a standard relation between a scattering matrix and its associated transfer matrix. We employ this relation, modified to include the phases χ_1, χ_2 on the top and bottom links, to obtain the transfer matrix

$$T = \frac{1}{W_{21}} \begin{pmatrix} -\det W & W_{11} \\ -W_{22} & 1 \end{pmatrix} \begin{pmatrix} e^{i\chi_1} & 0 \\ 0 & e^{-i\chi_2} \end{pmatrix}. \quad (15)$$

This describes evolution across one unit cell of the 1D network. Since $W_{21} = 0$ when orbits decouple, it is already evident that there is a singularity at the magic condition. Physical states are required by the periodicity of \mathbf{p} -space to be extended eigenstates of T , i.e. states with pure phase eigenvalues $e^{i\theta}$ where θ can be considered a pseudomomentum. After a choice of gauge is made and the phases are determined as a function of E_F and B , we can explicitly solve for the allowed bands. In the main text, we have chosen Landau gauge so that $\xi_1 = \xi_2 = \xi$ and $\chi_1 = \chi_2 = \chi$. It follows that

$$\chi = l_B^2 (S_0 - S_1)/2 \quad (16a)$$

$$\xi = l_B^2 S_1/2 + \pi/2 \quad (16b)$$

where we the areas S_0 and S_1 and $\tilde{\varphi}_S$ are defined in the main text. With this choice the determinant of T is unity and the eigenvalues satisfy

$$\cos \theta = \frac{1}{2} \text{Tr } T. \quad (17)$$

For parabolic dispersion, we make use of

$$P = e^{-\pi \Delta^2 / 4 E_F \omega_c \sin \alpha} \quad (18)$$

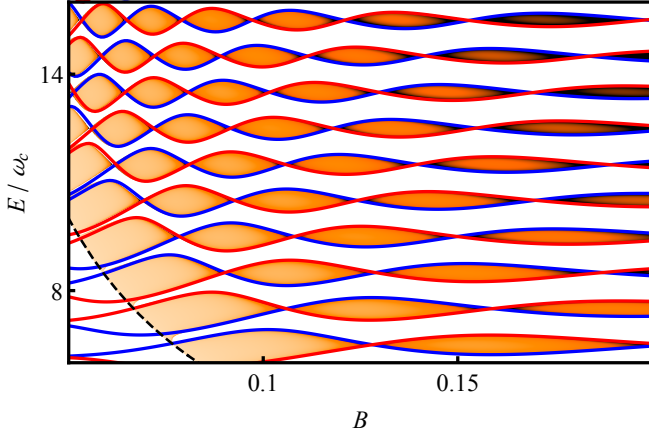


FIG. 3. Comparing the magnetic spectrum obtained using semiclassics (density plot) and exact diagonalization (red and blue lines, showing band tops and bottoms). Plotted for parabolic dispersion $p^2/2m$ in a periodic potential $V_0 \cos qx$ with $V_0 = 0.2, q = 2, m = 1$. For $E < q^2/8m$ (black dashed line) the orbits do not intersect and the semi-classical theory presented does not apply.

where $\alpha = 2 \sin^{-1} x$ and $x = q/2k_F$. The DOS can be explicitly obtained as $\rho(E_F, B) \propto |d\theta/dB|$. This model is closely related to the model considered by Pippard [?]; we have extended it by applying a the unitary U derived from first-principles (the precise form of which is important for recovering the perturbative limit), generalizing to arbitrary Fermi surface shape, extending to networks with many intersecting Fermi surfaces, including a Maslov correction to the spectrum, and extending, at least in part, to 2D networks at rational flux.

In Fig. 3, we compare the DOS obtained using this semiclassical method with exact diagonalization (ED). Below a certain energy, shown as a dashed line, the semiclassical network model consists of non-intersecting Fermi surfaces and no band broadening is predicted, in contrast with the ED. However, the semiclassical approach is only expected to be valid when the Fermi energy is much larger than the potential strength, and in this regime we find good agreement.

Density of states, 2D hexagonal network. We consider a periodic potential with six-fold symmetry and separate

the discussion into two cases, shown in in Fig. 4. When the network topology takes the form of Fig. 4a, the arguments in the main text apply and there are flat bands at the magic zero conditions, with the following caveat: the network model itself has a well-defined unit cell (in \mathbf{p} -space) only when the number of flux quanta per unit cell of real space is a rational number p/q . However, the flux at any magic zero can be approximated arbitrarily well by a rational, so this does not pose any problems. This discussion mirrors the discussion in the main text. The second case is when the network topology takes the form of Fig. 4b, which is relevant when the Fermi en-

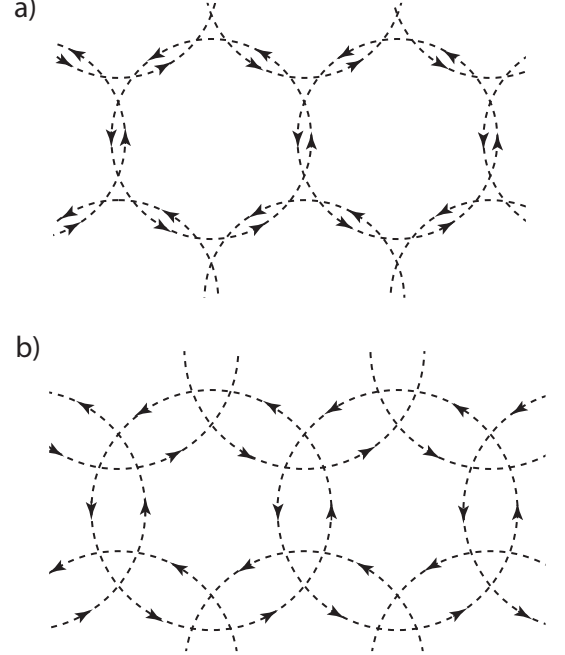


FIG. 4. Network model schematic in the case of a potential with six-fold symmetry when (a) lens orbits do not overlap and (b) lens orbits overlap.

ergy exceeds E_K , the energy at the K point of the mini BZ. The network has two pseudomomenta which we call θ_x, θ_y . When the number of flux quanta per unit cell is of the form $1/(2q)$ for integer q , the dispersion is captured by the following analog of Eq. (17):

$$C \equiv \sum_{i=1}^3 \cos \vartheta_i = \frac{\sin(\frac{1}{2}\mathcal{O}) - 2(1-P)^{3/2} \sin(\mathcal{O} - \frac{3}{2}\mathcal{L}) + (1-P)^3 \sin(\frac{3}{2}\mathcal{O} - 3\mathcal{L}) - 3P^2(1-P) \sin(\frac{1}{2}\mathcal{O} - \mathcal{L})}{2P\sqrt{1-P}[\sqrt{1-P} \sin(\frac{1}{2}\mathcal{O} - \mathcal{L}) - \sin(\frac{1}{2}\mathcal{L})]} \quad (19)$$

where $\vartheta_1 = \theta_x, \vartheta_2 = (-\theta_x - \sqrt{3}\theta_y)/2, \vartheta_3 = (-\theta_x + \sqrt{3}\theta_y)/2$ and

$$\mathcal{O} = l_B^2 S_0 + 2\pi\gamma, \quad (20a)$$

$$\mathcal{L} = l_B^2 S_1 + 2\tilde{\varphi}_S + 2\pi\gamma, \quad (20b)$$

are the original orbit and lens orbit Aharonov-Bohm phases, corrected by the Stokes phase and Maslov contributions. This result is adapted from Eq. 35 of Ref. [?], except that we've described scattering at junctions by the Landau-Zener unitary U and Ref. [?] lacked a first-principles calculation for this unitary.

We may note that C becomes singular when both \mathcal{O} and \mathcal{L} are integer multiples of 2π , and this is equivalent to the magic zero conditions in the main text. The bandwidth is zero whenever this condition is met. However, we are not currently aware of the generalization to all rational fluxes. When the number of flux quanta per unit cell is $p/(2q)$, the network model unit cell must be enlarged by a factor of p , and a difficult set of equations must be solved. However, it is reasonable to expect that the band envelopes of Eq. (19) are quite accurate at all flux values, while the exact solution of the network model only refines the subband structure [?]. While a proof of this is lacking, we note that there are still infinitely many magic zeros arbitrarily close to fluxes of the form $1/(2q)$; moreover, we proved in the main text that magic zeros are present when the network model consists of non-overlapping lens orbits.

Finally, we note that six-fold (or four-fold) symmetry of the potential is important. An anisotropic potential does not even lead to perfectly flat bands in the perturbative regime. Equal magnitude wavevectors is the most common scenario in moiré materials, however.

Hofstadter model. While both the Landau spectrum in a 2D moiré potential and the Hofstadter spectrum exhibit fractal-like features, our study considers Landau levels in a weak superlattice potential relative to bandwidth while the conventional Hofstadter model considers a single band in the tight-binding limit of deep potential. Moreover, perfectly flat bands are not present in the conventional Hofstadter model: while some bands become flat as the flux approaches an integer or half-integer, these bands also have vanishing spectral weight.

Weiss oscillations. Weiss oscillations show up in conductivity and magnetoresistance measurements in addition to the usual Shubnikov-de Haas (SdH) oscillations when a periodic potential is present [?]. The hallmark is that the DOS peaks when the cyclotron radius is commensurate with the period [? ? ? ? ?]:

$$2R_c = a(j - 1/4), \quad j = 1, 2, 3, \dots \quad (21)$$

where $R_c = k_F/eB$ for circular Fermi surfaces. It is simple to see that this is identical to the large n , perturbative result in the main text, which is derived within the semiclassical framework. The semiclassical description of the magic zeros as the intersection of two Landau fans, however, does not rely on any particular dispersion or on the perturbative limit.

Any SdH oscillation can be written as a quantization condition $l_B^2 S = 2\pi(j + \phi)$ where S is some \mathbf{p} -space area. Naturally, we may ask if there is an interpretation for

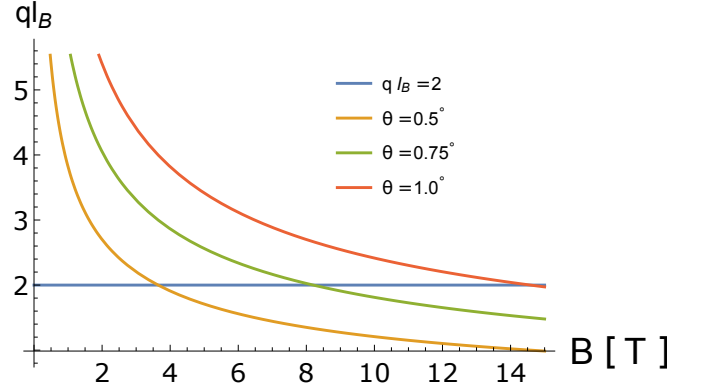


FIG. 5. Plots of ql_B for various twist angles (colored lines) in the chiral limit of TBG as well as the magic zeros in the 2nd and 3rd LLs. Various magic zeros are accessible at realistic fields.

Weiss oscillations in terms of a \mathbf{p} -space area, using the fact that Eq. (21) can be written

$$l_B^2(4k_F^2 x) = 2\pi(j - 1/4) \quad (22)$$

where $x = q/2k_F$. Indeed, it follows that

$$4k_F^2 x = S_0 - S_1 + O(n^{-1/2}) \quad (23)$$

(using $k_F \sim \sqrt{n}$) so in the large n limit our semiclassical model associates Weiss oscillations to the \mathbf{p} -space area $S_0 - S_1$. This is not the area of any semiclassical orbit, as would be the case for SdH oscillations, but rather the *difference* of such areas. A suggestive interpretation of the above is as follows. The magic zeros occur at the intersections of two Landau fans corresponding to oscillation frequencies S_0 and S_1 , respectively. Roughly speaking, the frequency of intersections of the two fans is then the difference of frequencies. Indeed, the observation of quantum oscillations which cannot be associated to any semiclassical orbit is expected when magnetic breakdown is taken into account [?].

APPLICATION TO TWISTED BILAYER GRAPHENE

In this section we investigate whether magic zeros arise in twisted bilayer graphene (TBG) in a uniform magnetic field. The spectrum of TBG is described by [?]

$$H = v(\mathbf{k} \cdot \boldsymbol{\sigma})\mathbb{I} + \begin{pmatrix} 0 & U(r) \\ U(r)^\dagger & 0 \end{pmatrix} \quad (24)$$

where $U(r) = \sum_{j=1}^3 U_n e^{i\mathbf{q}_j \cdot \mathbf{r}}$ where $\mathbf{q}_1 = q(0, 1)$ and $\mathbf{q}_{2,3} = q(\pm\sqrt{3}/2, -1/2)$ and

$$U_{j+1} = w_{AA}\sigma_0 + w_{AB}(\sigma_x \cos \frac{2\pi j}{3} + \sigma_y \sin \frac{2\pi j}{3}). \quad (25)$$

The Dirac Landau levels when $U = 0$ are

$$|n, \xi\rangle_D = \frac{1}{\sqrt{2}} \begin{pmatrix} |n\rangle \\ |n-1\rangle \end{pmatrix} \otimes |\xi\rangle_L \quad (26)$$

where $|\xi\rangle_L$ ($\xi = \pm 1$) is a layer eigenstate and $|n\rangle$ is a Schrödinger LL wavefunction. We've assume $n > 0$ for now. The potential projected into the n 'th Dirac LL is

$$\begin{pmatrix} 0 & \langle n, 1|U|n, 2\rangle_D \\ \langle n, 2|U^\dagger|n, 1\rangle_D & 0 \end{pmatrix} \quad (27)$$

where [?]]

$$\begin{aligned} \langle n, 1|U|n, 2\rangle_D &= \frac{1}{2} w_{AA} e^{-q^2 l_B^2/4} (L_n(q^2 l_B^2/2) + L_{n-1}(q^2 l_B^2/2)) \sum_{j=1}^3 e^{i\mathbf{q}_j \cdot \hat{\mathbf{r}}} \\ &+ \frac{1}{\sqrt{2}} w_{AB} e^{-q^2 l_B^2/4} q l_B L_{n-1}^{(1)}(q^2 l_B^2/2) \sum_{j=1}^3 \cos \frac{2\pi(j-1)}{3} e^{i2\pi(j-1)/3} e^{i\mathbf{q}_j \cdot \hat{\mathbf{r}}} \quad (28) \end{aligned}$$

where $\hat{\mathbf{r}} = (\hat{X}, -\hat{P})$ and $[\hat{X}, \hat{P}] = i l_B^2$. This can be extended to all levels by replacing n with $|n|$, with the convention $L_{-1}(x) = L_{-1}^{(1)}(x) = 0$. Let's take the chiral limit, $w_{AA} = 0$. Then it is clear that the projected potential vanishes whenever

$$L_{n-1}^{(1)}(q^2 l_B^2/2) = 0. \quad (29)$$

In the anti-chiral limit of $w_{AB} = 0$, the condition is

$$L_n(q^2 l_B^2/2) + L_{n-1}(q^2 l_B^2/2) = 0. \quad (30)$$

Examples of magic zero values for both limits are provided in Table I. In realistic TBG, it is possible that magic zeros corresponding to either of these two limits are broadened but still observable (see e.g. Fig. 1 of [?]).

We note that $q = \frac{8\pi}{3a_0} \sin \frac{\theta}{2}$ at small angles in TBG, where $a_0 = 0.246$ nm is the lattice constant of graphene. A useful relation is then $q l_B = 875.2 \sin \frac{\theta}{2} / \sqrt{B[\text{T}]}$. In Fig. 5 we plot this relation for various θ and compare to a few magic zeros. This indicates the “approximate magic zeros” are accessible at realistic magnetic fields.

$ n $	$q l_B$ (chiral limit)	$q l_B$ (anti-chiral limit)
1		2
2	2	1.24, 3.24
3	1.59, 3.08	0.99, 2.36, 4.18
4	1.37, 2.57, 3.94	0.86, 2, 3.26, 4.96
5	1.22, 2.27, 3.39, 4.68	0.76, 1.77, 2.84, 4.03, 5.65

TABLE I. Magic zero values of $q l_B$ for the n th Dirac Landau level in TBG, in the chiral and anti-chiral limits, at first order in perturbation theory.

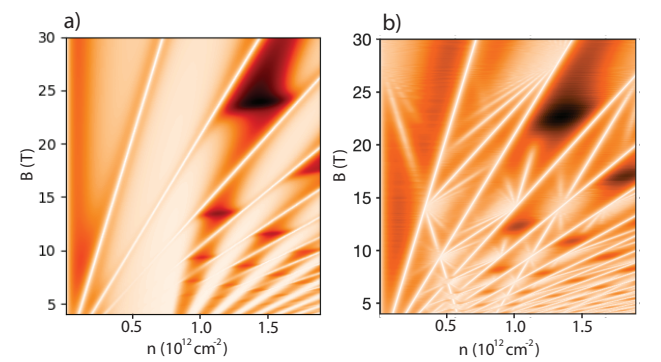


FIG. 6. Noninteracting compressibility as a function of density and B for a 1D potential (a) and 2D potential (b), at $T = 0.2$ meV. Magic zeros are dark features of high compressibility occurring over a finite range of n . Panel (b) exhibits Hofstadter-like features in addition to the magic zeros. Parameters match Fig. 1a and 1c, respectively.

COMPRESSIBILITY SIGNATURES

We include here some comments on the compressibility signatures of magic zeros. The flat bands due to magic zeros would naïvely lead to strong compressibility signatures. In Fig. 6 we plot the compressibility due to the magnetic spectrum in 1D and 2D moiré potential cases.

In real systems, however, interactions would destabilize these sharp features and possibly lead to interesting correlated states near the magic zeros. The nature of the correlated states near magic zeros is an interesting problem for future work.